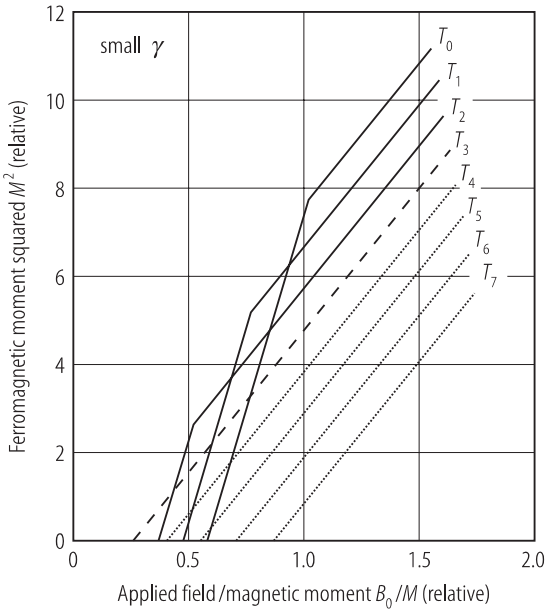

Fig. 72. Arrott plots for the case of weak coupling. The symbols and other parameters are identical to those of Fig. 70.

1.5.5.3.2.6 Discussion

The above analysis of some magnetic model systems has illustrated the potential of Landau theory and its application to the description of magnetic properties. With the help of Arrott plots the connection is made to the free energy. In favourable circumstances the parameters and their temperature dependence may be obtained from the experimental data by the use of Arrott plots. This allows a description of magnetic properties taking into account the knowledge of the system, and in particular its symmetry. If the symmetry of the magnetic structure is also known the modelling may be used to obtain a description of the effect of temperature and field on the stability of the arrangement of magnetic moments. For clarity, effects arising from fluctuations of the order parameter have been neglected. However, if important they can be incorporated into the present formulation in a straightforward manner. Other possible complications such as the presence of crystal fields have been dealt with elsewhere [95N3].

1.5.5.3.3 Experimental results

The majority of the magnetic properties have already been reviewed in [88W1]. Those which have appeared since are primarily more detailed examinations of the effect of atomic order or new compounds containing rare-earth elements.

1.5.5.3.3.1 Ferromagnets

X_2YZ X = 3d, Y = 3d

X = 8A: Ni; 1B: Cu
Y = 7A: Mn
Z = 3B: Al, Ga, In; 4B: Sn

Alloys in the series Cu_2MnZ and Ni_2MnZ are, with the exception of Ni_2MnAl, ferromagnetic [88W1]. The compounds form the Heusler $L2_1$ structure and a moment of approximately $4\mu_B$ is

confined to the Mn atoms. Recently Cu_2MnZ alloys have been prepared in the amorphous state by r.f. sputtering [83K1]. Spin glass freezing has been investigated in Cu_2MnZn alloys where the cusp occurs at temperatures an order of magnitude smaller than the Curie temperatures of crystalline samples.

Cu_2MnZ: Amorphous alloys

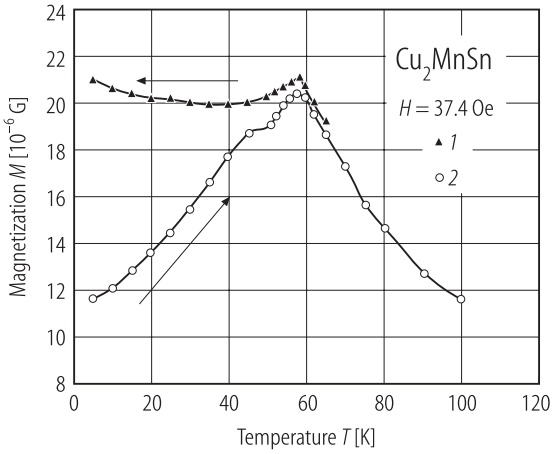

Fig. 73. Magnetisation M of an amorphous Cu_2MnSn film ($V = 5.025 \cdot 10^{-4}$ cm^3) in a measuring dc field of 37.4 Oe. The data points *1* were measured in order of decreasing temperature as indicated by the arrow. The data points *2* were taken upon increasing temperature, after the sample was cooled to 4.2 K in the field $H_{initial}$ = 13.2 Oe [83K3].

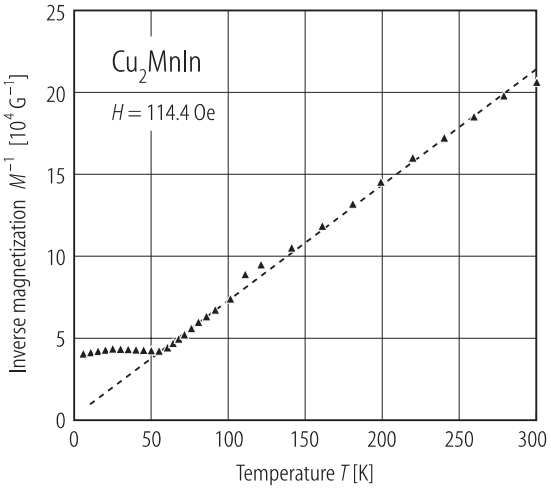

Fig. 74. Inverse magnetisation M^{-1} of an amorphous Cu_2MnIn film ($V = 1.69 \cdot 10^{-4}$ cm^3) in a dc field of 114.4 Oe. The Curie-Weiss behaviour is observed for all temperatures higher than T_{SG}.
p_{eff} = 3.5 μ_B, Θ = – 2.6 K [83K3].

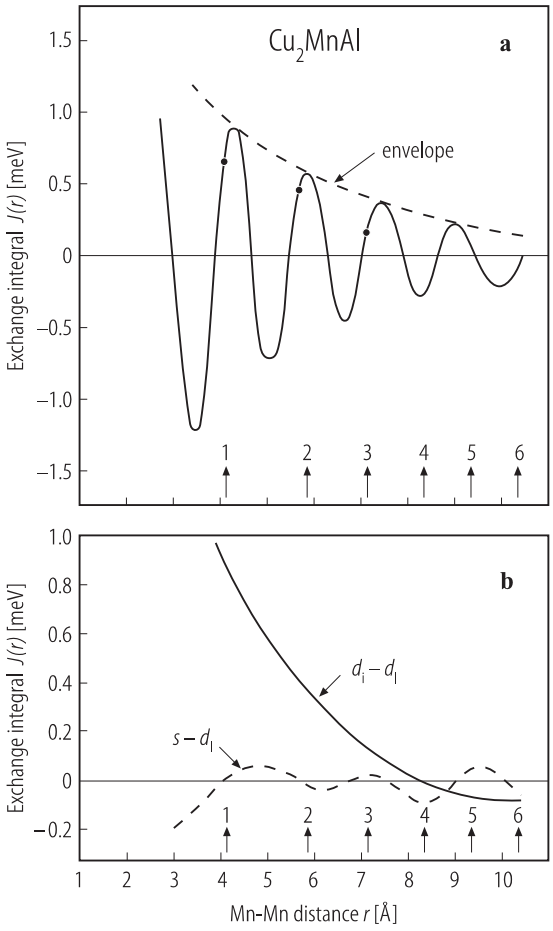

Fig. 75. Theoretical distance dependence of Mn-Mn exchange interactions $J(r)$ in Cu_2MnAl based on an RKKY model. The numbers refer to the nearest neighbour shells [83K3]. (**a**) The dashed line is Price's [78P1] result scaled in amplitude to match the experimental exchange interactions. (**b**) Varation of the itinerant-d-local-d exchange interactions.

Ni-Mn-Z: Crystalline alloys

The pressure dependence of the Curie temperature has been investigated in Ni_2MnZ alloys. For all compounds, the Curie temperatures increase linearly with pressure. Ni_2MnGa undergoes a martensitic phase transition at 202 K, the details of which are sensitive to the application of pressure. The effects of stoichiometry on the magnetic properties have been investigated in $Ni_{3-x}Mn_xSn$.

Table 15. A summary of the magnetic properties of Ni_2MnZ alloys [87K1].

Compound	a [Å]	T_C [K]	Θ [K]	p_{eff} [μ_B]	p_{Mn} [μ_{BJ}]
Ni_2MnAl	5.824	317	160	4.90	4.0
Ni_2MnGa	5.805	355	374	4.59	3.7
Ni_2MnIn	6.070	315	350	4.69	3.8
Ni_2MnSn	6.048	328	355	5.00	4.1
Ni_2MnSb	6.027	331	400	4.20	3.3

Table 16. Pressure coefficient of the Curie temperature for Ni_2MnZ alloys [87K1].

Compound	$(1/T_C)\,(dT_C/dp)$ [kbar^{-1}]
Ni_2MnAl	$+ 2.27\cdot10^{-3}$
Ni_2MnGa	$+ 2.82\cdot10^{-3}$
Ni_2MnIn	$+ 2.86\cdot10^{-3}$
Ni_2MnSn	$+ 4.27\cdot10^{-3}$
Ni_2MnSb	$+ 12.0\cdot10^{-3}$

Table 17. Lattice constant a, Curie temperature T_C and magnetic moments p in various Heusler alloys of the type $Ni_{3-x}Mn_xSn$. The values denoted by T_C were derived from DSC measurements [84B1].

x	a [nm]	T_C [K]	T_C' [K]	p_s [μ_B/f.u.]	p_{Mn} [μ_B]	p_{eff} [μ_B/Mn]
0.60	0.5992	200		2.51	4.18	
0.80	0.6028	275		3.40	4.25	
0.90	0.6045	324	312	3.82	4.24	
1.00	0.6048	362	342	4.24	4.24	5.07
1.10	0.6045	379	356	4.38	3.98	
1.25	0.6050	373	362	4.11	3.28	
1.30	0.6052	392	369	4.02	3.09	
1.40	0.6059	401	381	3.86	2.76	
1.60	0.6078	455	431	3.37	2.11	
1.70	0.6086	485	459	3.19	1.88	2.89
2.20	0.6131	557		1.90	0.86	

Table 18. The magnetic moment of Mn and Ni in the cubic and tetragonal phase [92O1].

	p_{Mn} [μ_B]		p_{Ni} [μ_B]	
	cub	tetr	cub	tetr
Experiment	3.41	3.41	0.56	0.41
Calculation	3.44	3.41	0.29	0.24

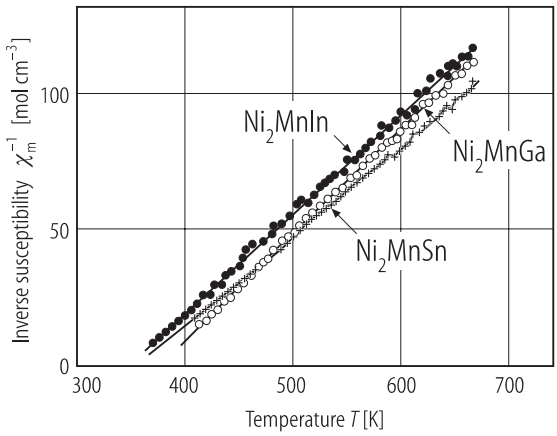

Fig. 76. Ni_2MnZ (Z = Ga, In and Sn). Inverse susceptibility vs. temperature curves [87K1].

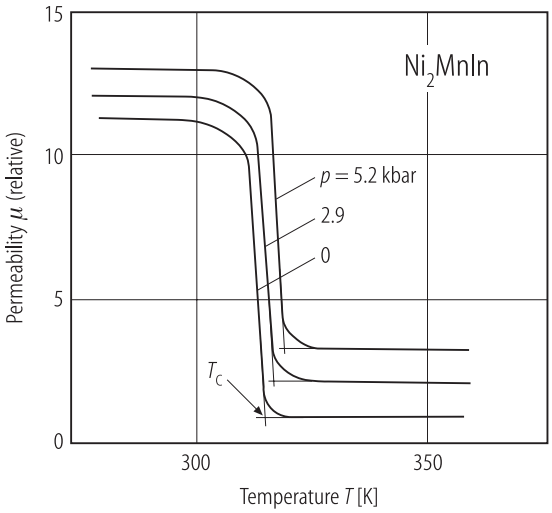

Fig. 77. Variation of permeability vs. temperature under hydrostatic pressure for Ni_2MnIn [87K1]. T_C : Curie temperature.

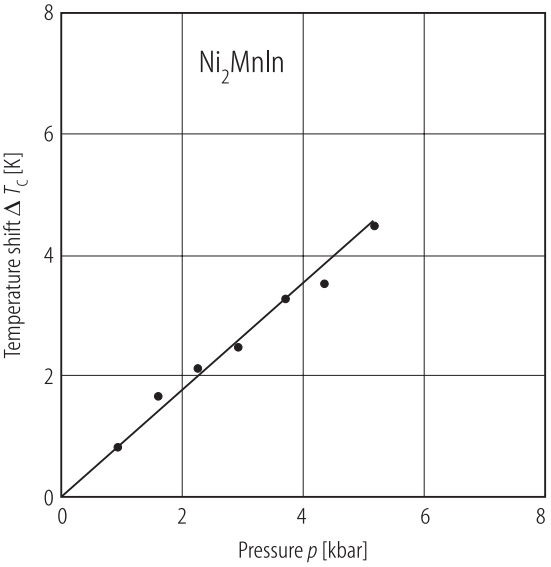

Fig. 78. Variation of the Curie temperature as a function of applied pressure for Ni_2MnIn [87K1].

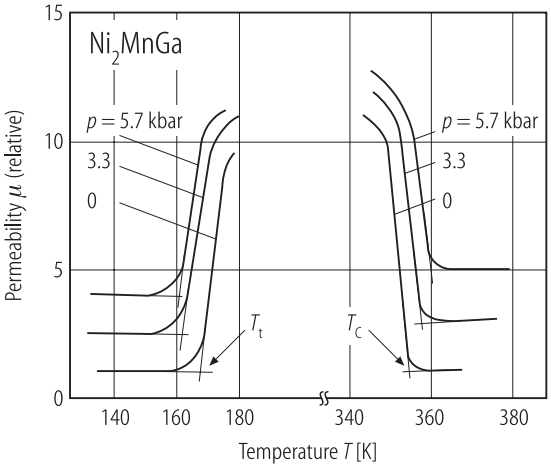

Fig. 79. Variation of permeability vs. temperature under hydrostatic pressure for Ni_2MnGa [87K1]. T_C : Curie temperature, T_t: structural phase transition temperature.

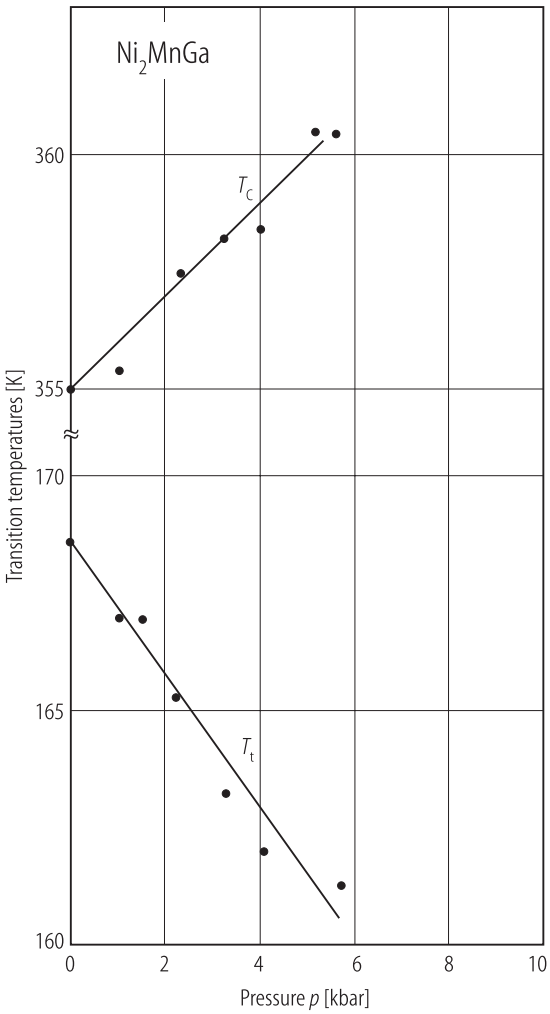

Fig. 80. Curie temperature T_C and the structural phase transition temperature T_t vs. pressure curves for Ni_2MnGa [87K1].

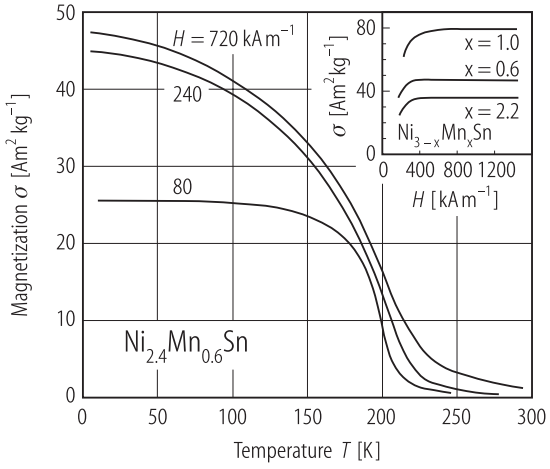

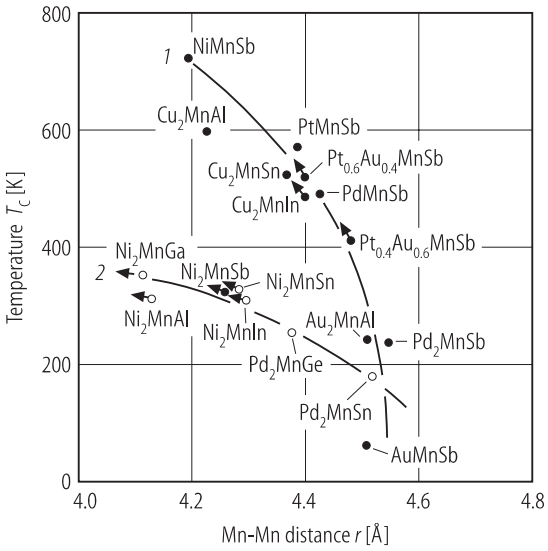

Fig. 81. Relation between the Mn-Mn distance and the Curie temperature for $L2_1$ and $C1_b$-type alloys. The arrows show the variation of T_C with pressure (an upward arrow indicates an increase) [87K1].

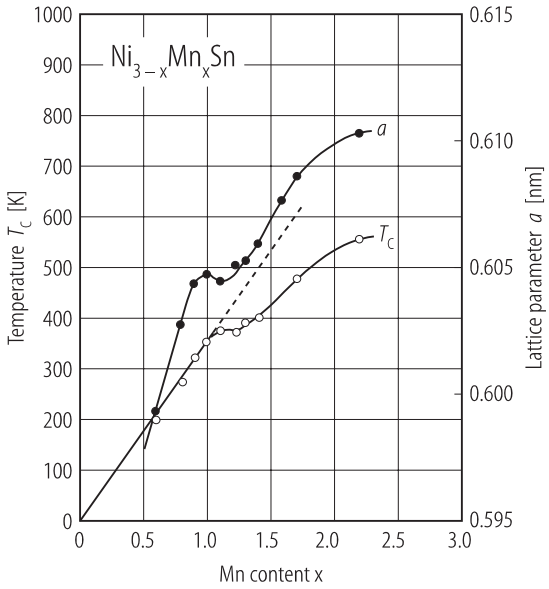

Fig. 83. Concentration dependence of the lattice constant a and the Curie temperature T_C in $Ni_{3-x}Mn_xSn$ [84B1].

Fig. 82. Temperature dependence of the magnetisation σ in $Ni_{2.4}Mn_{0.6}Sn$ for three different field strengths (H = 80, 240 and 720 kA/m). The inset shows the field dependence of σ for three $Ni_{3-x}Mn_xSn$ compounds at 4.2 K [84B1].

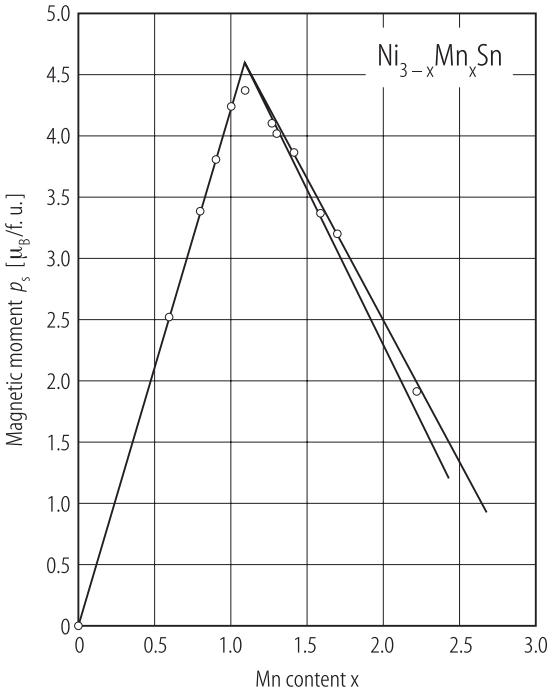

Fig. 84. Concentration dependence of the saturation moment p_s in the alloys $Ni_{3-x}Mn_xSn$. Included is a data point for Ni_3Sn, which is nonmagnetic but has a different crystal structure from the Heusler alloys. The full line represents the concentration dependence of p_s obtained by model calculations [84B1].

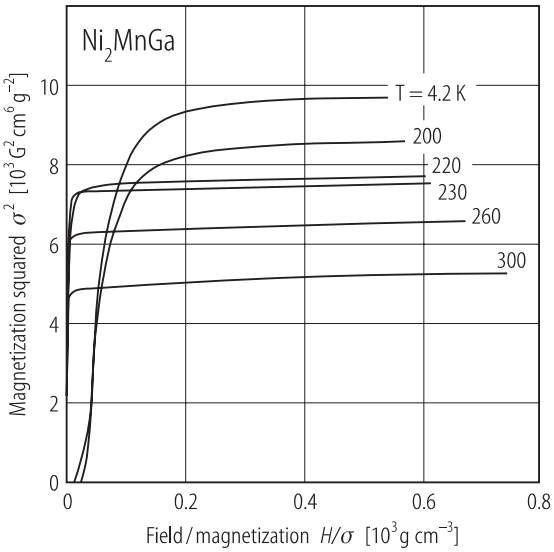

Fig. 85. Arrott plots for Ni_2MnGa with isotherms extending from 4.2 to 300 K. At approximately 202 K the crystal transforms martensitically. At room temperature the compound has the $L2_1$ structure [92O1].

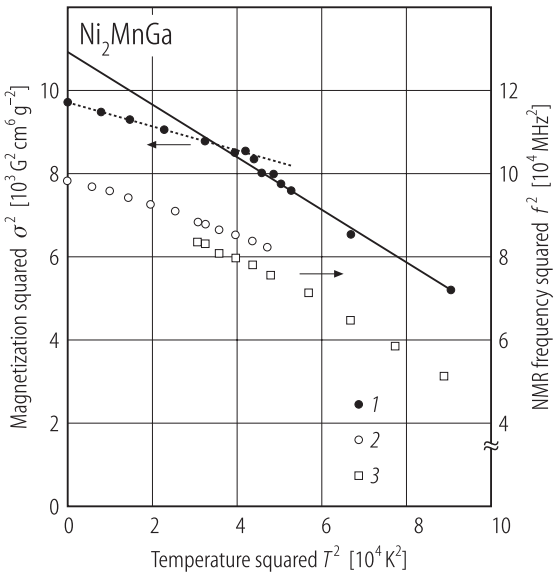

Fig. 86. Ni_2MnGa. Closed circles (*1*) show σ^2 vs. T^2 plots and *2* and *3* show the NMR frequency in f^2 vs. T^2 plots. *2* and *3* correspond to the cubic and tetragonal state respectively [92O1].

X_2YZ X = 3d

X = 7A: Mn; 8A: Fe, Co, Ni; 1B: Cu
Y = 4A: Ti, Zr, Hf; 5A: V, Nb, Ta; 6A: W; 7A: Mn
Z = 3B: Al, Ga; 4B: Si, Ge, Sn

Co_2YZ

The magnetic properties of Heusler alloys containing group 4A and 5A elements have previously been reported [73W1, 74Z1]. In all cases the moments were confined to the cobalt atoms. A systematic trend could be identified with the moment per formula unit being either significantly less than or greater than unity. Those compounds with Y = 4A and Z = 4B or 5A and 3B elements have the larger moments and those with 4A and 3B or 5A and 4B elements have smaller moments. If Y represents Mn, then compounds with high Curie temperatures are formed, in which both the cobalt and manganese atoms possess magnetic moments. Again, the moments per formula unit fall into two groups depending on the Z atom. For this series, the compounds with Z = 4B elements have higher moments, $\approx 5\mu_B$, than those with 3B elements, $\approx 4\mu_B$.

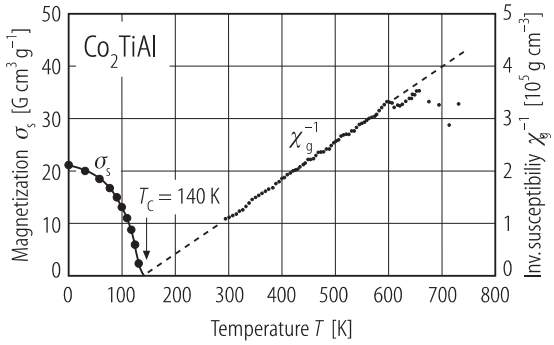

Fig. 87. Thermal variation of the magnetisation and inverse susceptibility for Co_2TiAl [92K1].

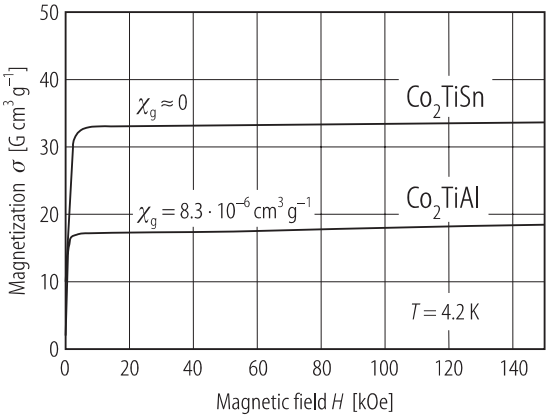

Fig. 88. Magnetisation vs. applied field at 4.2 K for Co_2TiAl and Co_2TiSn [92K1].

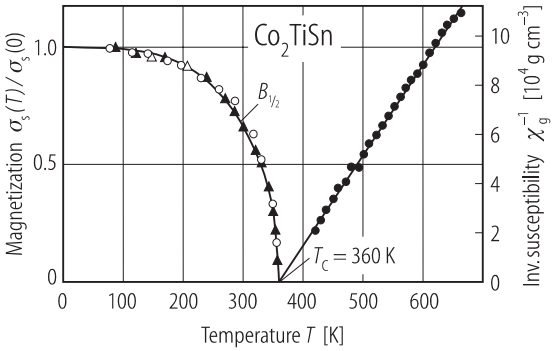

Fig. 89. Temperature dependence of the saturation magnetisation and reciprocal susceptibility of Co_2TiSn [92K1]. $\sigma_s(0)$ = 39.0 G cm^3g^{-1}, $2S_{Co}$ = 0.99; Θ = 360 K, $2S_{Co}$ = 1.01. $B_{1/2}$ denotes the Brillouin function for J = 1/2.

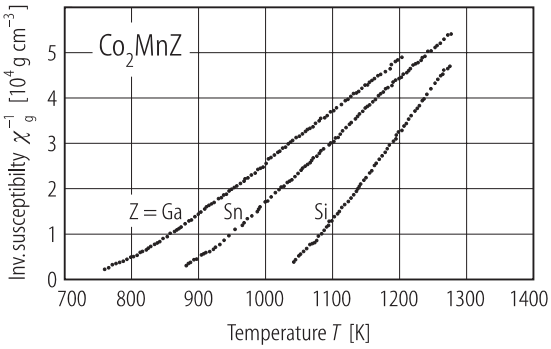

Fig. 90. Reciprocal susceptibility vs. temperature of Co_2MnZ alloys [88I1].

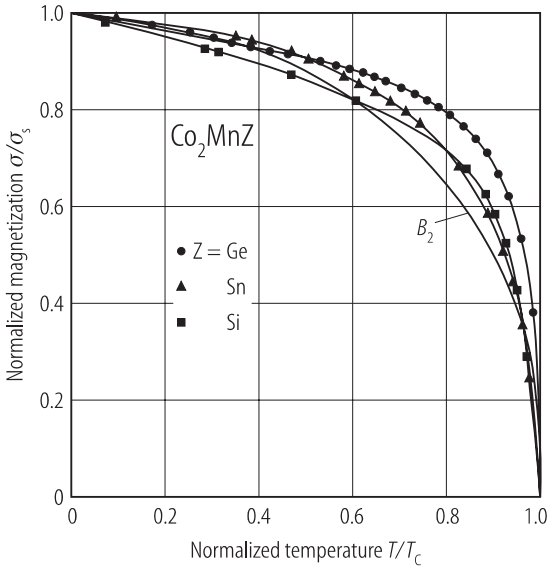

Fig. 91. Spontaneous magnetisation vs. temperature curves in the normalised form for Co_2MnZ (Z = Si, Ge, Sn) [86I1]. B_2 denotes the Brillouin function for $J = 2$.

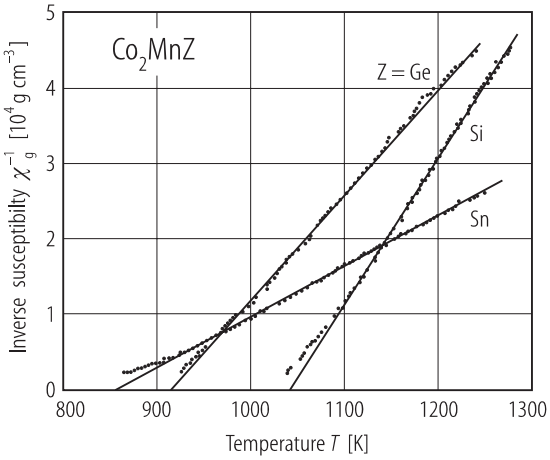

Fig. 92. Reciprocal susceptibility vs. temperature curves for Co_2MnZ (Z = Si, Ge, Sn). Z = Ge: p_{eff} = 2.82 μ_B/f.u., Θ = 912 K , T_C = 905 K; Sn: p_{eff} = 4.92μ_B/f.u., Θ = 860 K, T_C = 824.5 K; Si: p_{eff} = 2.03 μ_B/f.u., Θ = 1044 K, T_C = 1009.6 K [86I1].

Table 19. Magnetic and structural data for Co_2MnZ alloys [88I1].

Alloy	a [Å]	T_C [K]	Θ [K]	p_s [μ_B/f.u.]	p_{eff} [μ_B/f.u.]
Co_2MnSi	5.65	1034	1044	5.10	2.03
Co_2MnGe	5.74	905	890	4.66	2.61
Co_2MnSn	6.00	826	870	5.37	3.35
Co_2MnGa	5.77	695	770	4.09	3.28

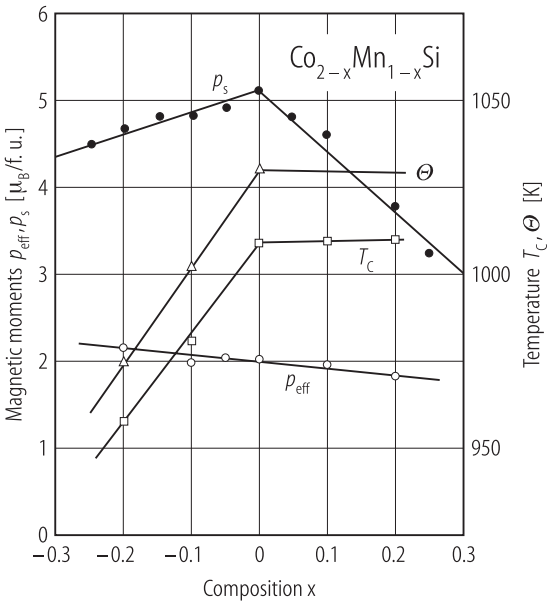

Fig. 93. Variation of T_C, Θ and p_s, p_{eff} with composition x in $Co_{2-x}Mn_{1-x}Si$ [88I1].

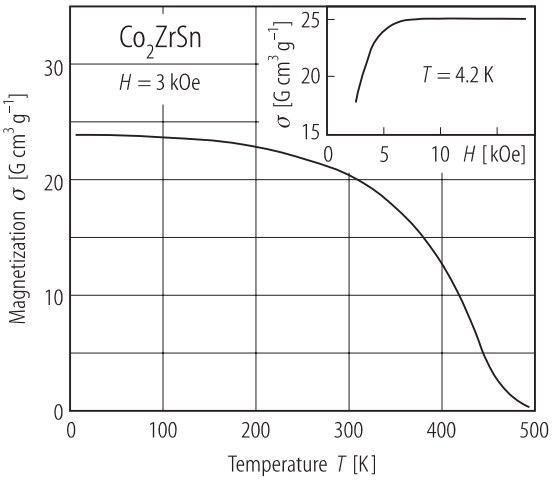

Fig. 94. Temperature dependence of the magnetisation σ measured in 3 kOe in Co_2ZrSn. The inset shows the field dependence of the magnetisation at 4.2 K [83V2].

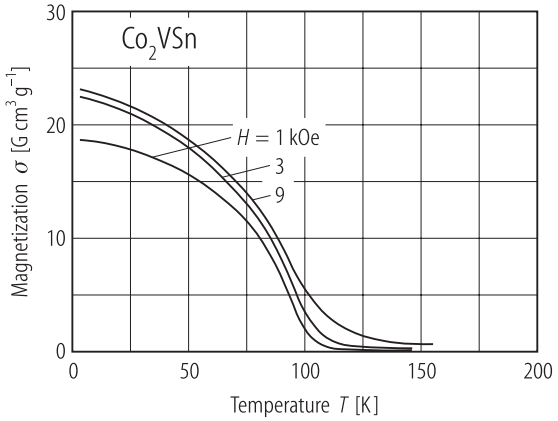

Fig. 95. Temperature dependence of the magnetisation σ observed in applied fields of 1, 3 and 9 kOe in Co_2VSn [83V2].

Fe_2MnSi

The compound Fe_2MnSi orders magnetically at 214 K and it is ferromagnetic down to 69 K [88W1]. Below this temperature a magnetic transition to a canted structure occurs, lowering the spontaneous magnetisation. X-ray diffraction measurements failed to reveal a magneto-volume effect at T_C.

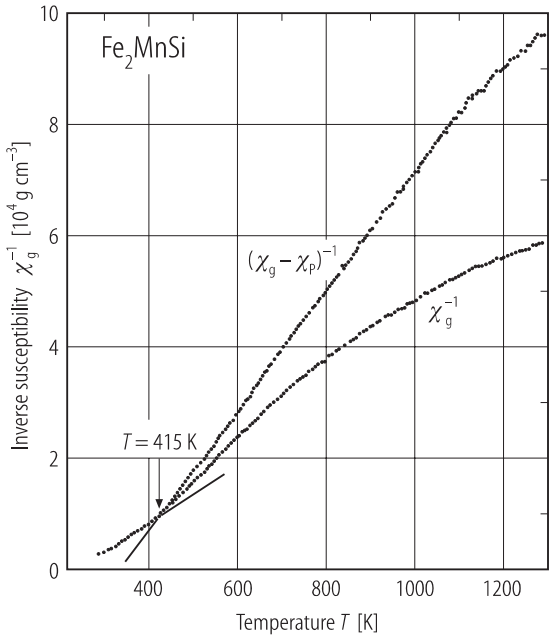

Fig. 96. Temperature dependence of the reciprocal susceptibility in Fe_2MnSi. The Pauli paramagnetic contribution χ_P was taken to be $6.6 \cdot 10^{-6}$ cm^3 g^{-1}. p_{eff} = 2.9 μ_B, Θ = 335 K [88K1].

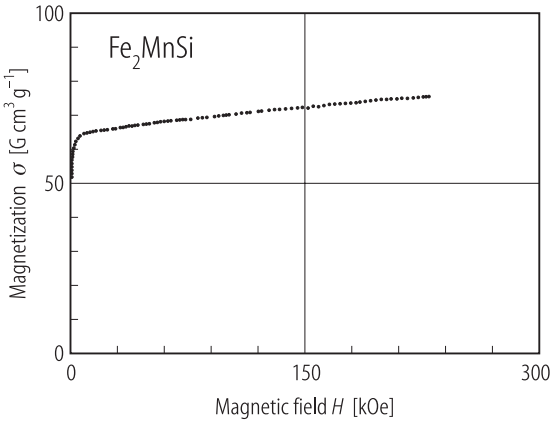

Fig. 98. High field magnetisation process at 4.2 K in Fe_2MnSi [88K1].

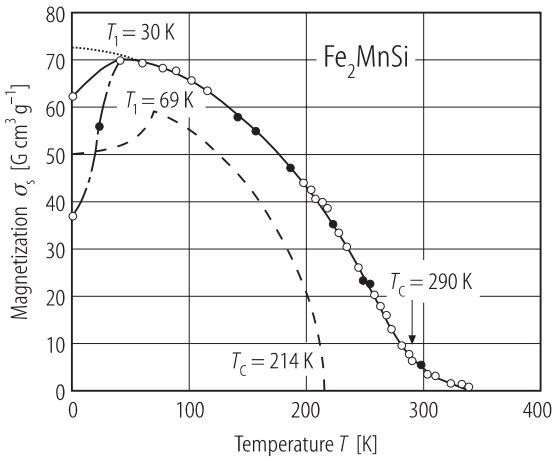

Fig. 97. Temperature dependence of spontaneous magnetisation (solid curve), magnetisation taken from [88K1] (dashed-dotted curve). Dotted curve: after heating the sample above the Curie temperature [88K1]. Dashed curve [76Z1].

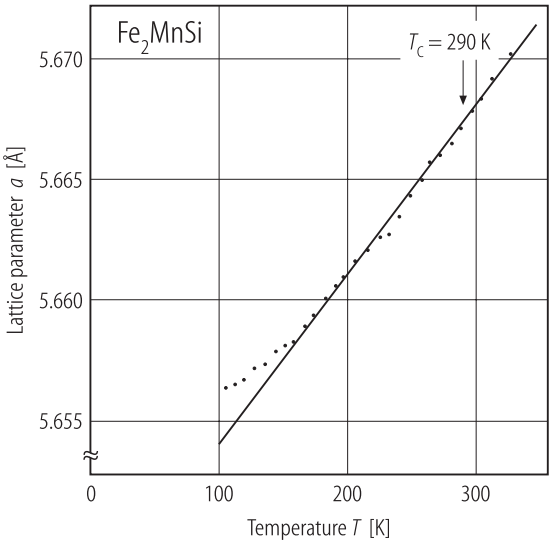

Fig. 99. Temperature dependence of the lattice constant of Fe_2MnSi. The high Curie temperature compared to other investigations may arise from a slightly different stoichiometry or atomic order [88K1].

Summary of the magnetic properties of Heusler alloys containing Sn.

Table 20. A summary of magnetic properties of X_2YSn Heusler alloys [83V2].

Compound	Heat treatment	a [Å]	T_C [K]	χ_g [10^{-6} cm^3 g^{-1}]	p [μ_B/f.u.]
Mn_2WSn	20 d 700 °C	6.317	258		1.54
Fe_2TiSn	as-cast	6.053		5.7	
Fe_2VSn	50 d 600 °C	5.959	200		1.32
Co_2TiSn	30 d 800 °C	6.076	371		1.96
Co_2ZrSn	20 h 900 °C	6.242	448		1.46
Co_2HfSn	11 d 800 °C	6.227	394		1.55
Co_2VSn	14 d 800 °C	5.960	95		1.21
Co_2NbSn	60 d 600 °C	6.142	105		0.69
Co_2MnSn	10 d 800 °C	5.984	829		4.79
Ni_2TiSn	4 d 800 °C	6.096		0.7	
Ni_2ZrSn	30 d 800 °C	6.276		0.9	
Ni_2HfSn	30 d 800 °C	6.240		0.7	
Ni_2VSn	4 d 800 °C	6.04		1.7	
Ni_2NbSn	30 d 800 °C	6.156		0.8	
Ni_2MnSn	30 d 800 °C	6.048	345		4.01
Cu_2MnSn	20 d 640 °C	6.168	530		3.97

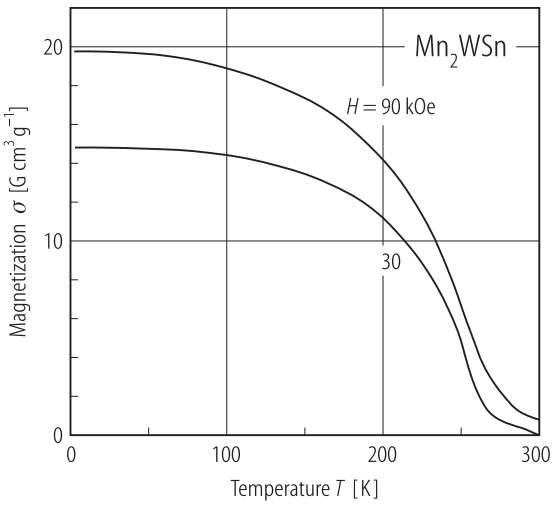

Fig. 100. Temperature dependence of the magnetisation σ measured in Mn_2WSn in 30 and 90 kOe [83V2].

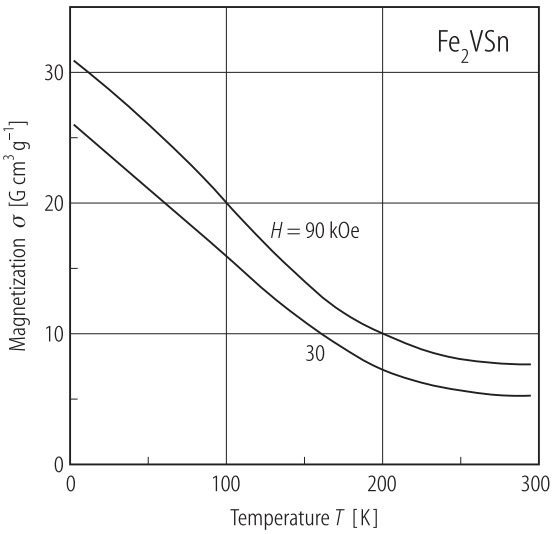

Fig. 101. Temperature dependence of the magnetisation σ measured in Fe_2VSn in 30 and 90 kOe [83V2].

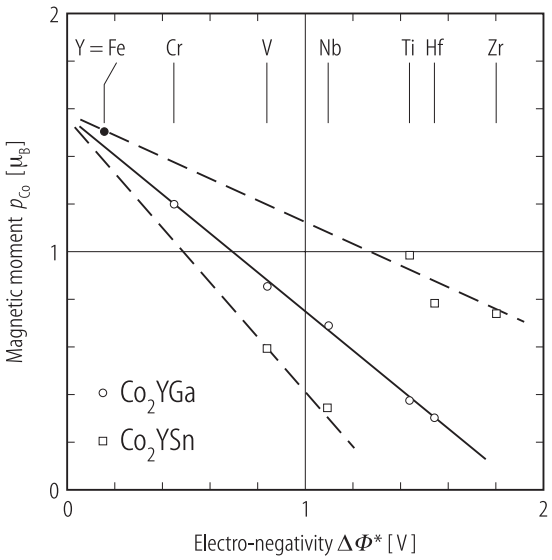

Fig. 102. Dependence of the Co moment (p_{Co}) in various Co_2YGa compounds (circles) and in various Co_2YSn compounds (squares) on the corresponding electro-negativity between $\Delta\Phi^*$ Co and the Y component [83V2].

$Fe_{3-x}V_xGe$

For $x \geq 0.4$, the alloys have the $L2_1$ structure. The magnetisation, magnetic moment per Fe site and Curie temperature all decrease with increasing x. These results, when taken with susceptibility measurements, have been interpreted as indicating itinerant behaviour.

Table 21. A summary of the magnetic properties of $Fe_{3-x}V_xGe$ alloys [90B1].

	C_g [10^{-3} cm^3 K g^{-1}]	q_c	q_s	q_c/q_s	T_C [K]	Θ [K]	$\sigma_{0.0}$ [G cm^3 g^{-1}]	p_{Fe} [μ_B]
$D0_{19}$ (Ni_3Sn) structures								
Fe_3Ge	21.45	5.50	6.43	0.86	634	655	149.5	2.14
$Fe_{2.8}V_{0.2}Ge$	21.32	5.46	5.74	0.95	559	572	134.0	2.05
$Fe_{2.6}V_{0.4}Ge$	20.2	5.28	4.89	1.08	476	498	114.6	1.88
$L2_1$ structures								
$Fe_{2.4}V_{0.6}Ge$	11.8	3.85	2.40	1.60	459	510	56.6	1.00
$Fe_{2.2}V_{0.8}Ge$	8.62	3.16	1.25	2.52	255	366	29.5	0.56
$Fe_{2.0}V_{1.0}Ge$ [1])			0.72		170		17.0	0.36

[1]) Alloy with second phase.

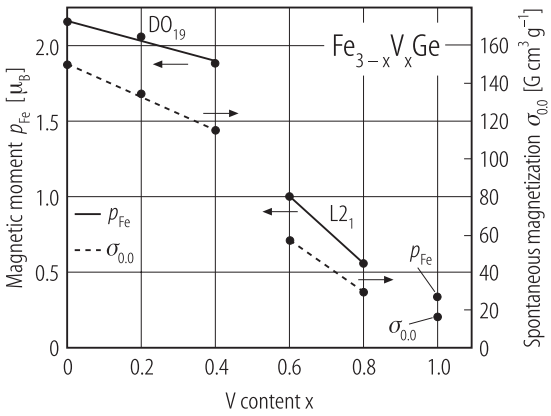

Fig. 103. Variation in spontaneous magnetisation at 0 K, $\sigma_{0,0}$, and magnetic moment p_{Fe} per Fe atom vs. x for $Fe_{3-x}V_xGe$ alloys [90B1].

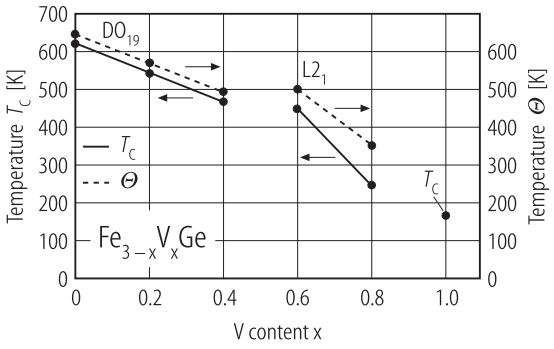

Fig. 104. Variation in the ferromagnetic Curie temperature T_C and the paramagnetic Curie temperature Θ vs. x for $Fe_{3-x}V_xGe$ alloys [90B1].

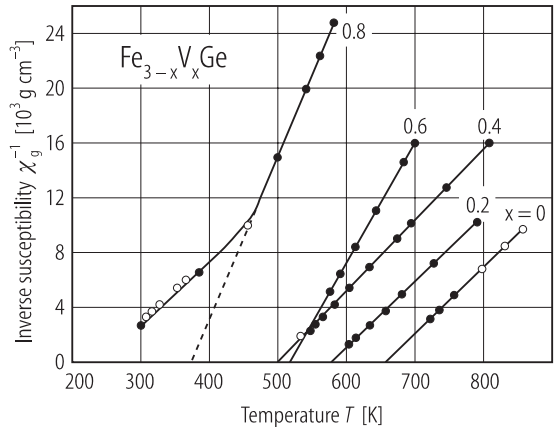

Fig. 105. Inverse susceptibility χ_g^{-1} vs. temperature for $Fe_{3-x}V_xGe$ alloys [90B1].

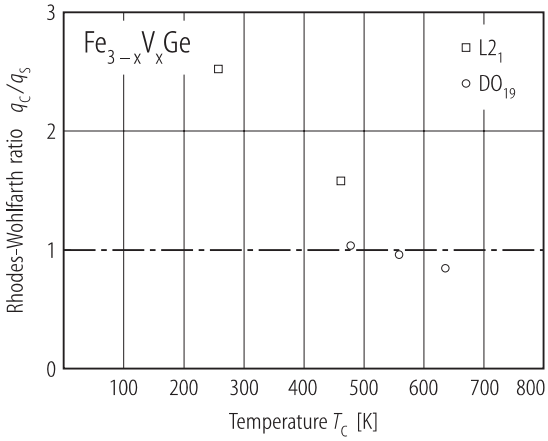

Fig. 106. Rhodes-Wohlfarth plot q_c/q_s [63R1] vs. Curie temperature for $Fe_{3-x}V_xG$ alloys. For a localised system $q_c/q_s = 1$ [90B1]. q_c and q_s being defined by the equations $p_{eff}^2 = q_c(q_c + 2)\mu_B^2$ and $p_m = q_s\mu_B$, respectively.

X_2YZ X = 3d, 4d, Y = 3d

X = 8A: Ni, Pd
Y = 4A: Ti; 7A: Mn
Z = 3B: Al, Ga, In; 4B: Sn

Pd_2MnSn

The magnetisation in Pd_2MnSn Heusler decreases drastically by heavy plastic deformation. However, the loss in magnetisation can be recovered by annealing in the temperature range between 300 °C and 800 °C. The Mn atoms near the antiphase boundaries have a different atomic environment from the ordered state, producing a different exchange constant.

Table 22. Number of Mn neighbours around a Mn atom at the j^{th} nearest neighbour distance r_j in the normal state and on the 0, I, II and III planes very close to APB(1) and APB (2) in the Heusler ($L2_1$) type alloys and the B2 and A2 type alloys [84I1].

j^{th} nearest-neighbour sites			1	2	3	4	5	6	7	8	9	10	11	12	13	14	15	16	17
$(4r_j/a_0)^2$			3	4	8	11	12	16	19	20	24	27	32	35	36	40	43	44	48
Total number of atom pairs			8	6	12	24	8	6	24	24	24	32	12	48	30	24	24	24	6
z_j	$L2_l$-type	Normal state	0	0	12	0	0	6	0	0	24	0	12	0	0	24	0	0	8
		APB(1) 0 plane	1	0	7	5	0	4	5	0	14	6	7	12	0	12	5	0	6
		I plane	0	0	11	2	0	4	3	0	18	5	7	8	0	16	3	0	6
		II plane	0	0	12	0	0	6	1	0	20	3	11	4	0	16	3	0	6
		III plane	0	0	12	0	0	6	0	0	24	0	11	2	0	22	2	0	6
		APB(2) 0 plane	0	2	7	0	2	4	0	12	14	0	7	0	12	12	0	10	6
		I plane	0	0	11	0	2	4	0	6	18	0	7	0	8	16	0	10	6
		II plane	0	0	12	0	0	6	0	2	20	0	11	0	8	18	0	4	6
		III plane	0	0	12	0	0	6	0	0	24	0	11	0	2	22	0	4	6
	B2-type		0	3	6	0	4	3	0	12	12	0	6	0	15	12	0	12	4
	A2-type		2	3/2	3	6	2	3/2	6	6	6	8	3	12	15/2	6	6	6	2

Table 23. Magnetic interactions on the Mn atoms in the normal state and on the 0, I, II and III planes near APB(1) and APB(2) in Pd_2MnSn calculated form the experimental $J(r)$ curves with an accuracy of 10 % (see Fig. 111). Units are meV, except for the $J(i)/J(N)$ values (in %) [84I1].

Magnetic interaction	Pd_2MnSn	Ni_2MnSn
$J(N)$	4.16	7.18
J(1-0)	– 2.97	– 1.35
J(1-I)	3.92	6.93
J(1-II)	3.67	6.72
J(1-III)	4.19	7.12
J(2-0)	1.67	5.58
J(2-I)	4.34	7.36
J(2-II)	3.89	6.66
J(2-III)	4.23	7.15
$\Delta J(1)/J(N)$	– 1.88	– 1.30
$\Delta J(2)/J(N)$	– 0.61	– 0.28

Table 24. Experimental results of the cold-working effect on some magnetic properties in the Pd_2MnSn alloy. Sample no. 1 is as-crushed and samples 2 and 3 are annealed at 300 °C and 400 °C respectively for 10 h after crushing. M_0^I and M_0^{II} are estimated from (almost straight) parts of the magnetization curve at T = 4.2 K for fields ≥ 2.6 T and 5.5 T, respectively [84I1].

Sample	$\Delta\Theta_m/\Theta_m(N)$ [%]	$\Delta C_m/C_m(N)$ [%]	$\Delta M_0^I/M_0(N)$ [%]	χ_{HF} [10^{-3} cm^3 mol^{-1}]	$\Delta M_0^{II}/M_0(N)$ [%]
1	– 8 ± 1	– 26 ± 1	– 59 ± 1	9.3 ± 0.4	– 33 ± 2
2	+ 1 ± 1	– 17 ± 1	– 43 ± 1	11.8 ± 0.4	– 16 ± 1
3			– 21 ± 1	4.3 ± 0.4	– 13 ± 1

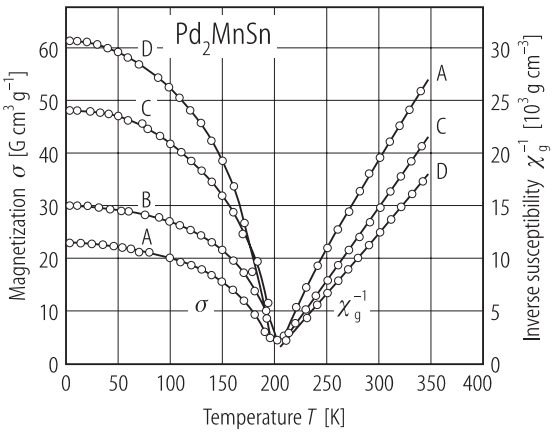

Fig. 107. Magnetisation and reciprocal susceptibility as a function of temperature for Pd_2MnSn with different heat treatment. (A) specimen crushed but not annealed, (B), (C) and (D) the same specimen annealed for 10h at 300, 500 and 800°C respectively. A, B and C were measured in 7.7 kOe and D in 5.8 kOe [83T1].

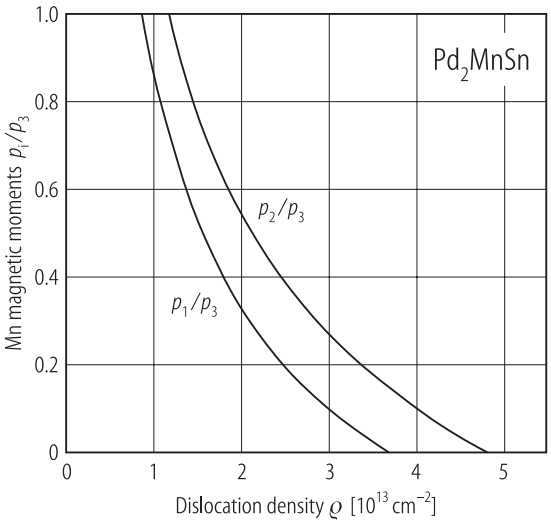

Fig. 108. Relation between the magnetic moment of Mn atoms in Pd_2MnSn at the irregular sites and the dislocation density in crushed specimen. The subscript 3 refers to regular sites and 1 and 2 to the irregular sites [83T1].

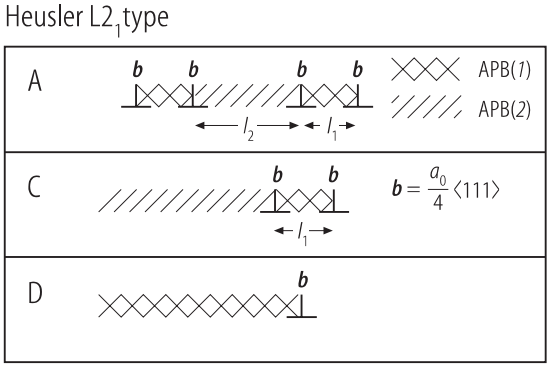

Fig. 109. Superlattice dislocation configurations of the Heusler ($L2_1$ type) alloy. The notation A, C, D is employed to describe three types of superlattice dislocations [84I1]. APB: antiphase boundary.

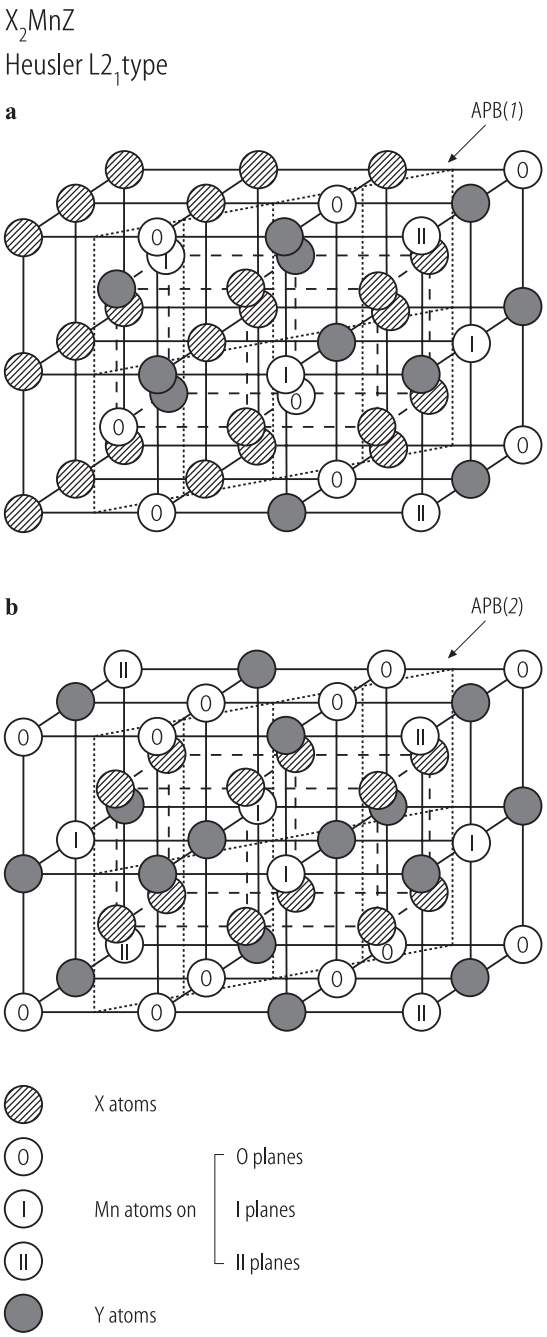

Fig. 110. Atomic arrangements of the Heusler ($L2_1$ type) structure after the (**a**) $a_0/4$ <111> and (**b**) $a_0/2$ <111> dislocations have slipped the {110} glide plane and created antiphase boundaries APB (*1*) and APB (*2*) respectively [84I1].

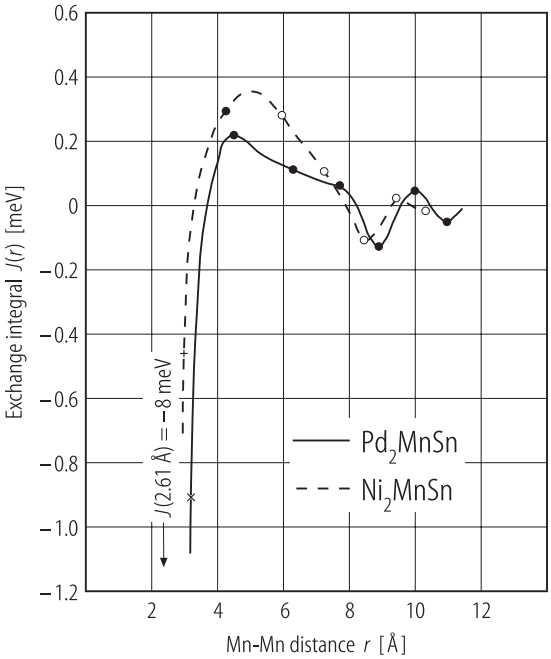

Fig. 111. Exchange interactions between Mn atoms in two ferromagnetic alloys Pd_2MnSn and Ni_2MnSn [84I1].

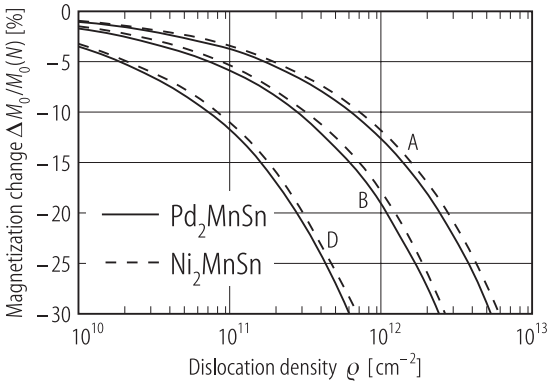

Fig. 112. Variation rate of the spontaneous magnetisation at 0 K by plastic deformation. $\Delta M_0/M_0(N)$ as a function of the dislocation density ρ in Pd_2MnSn and Ni_2MnSn. N refers to the normal undeformed state [84I1].

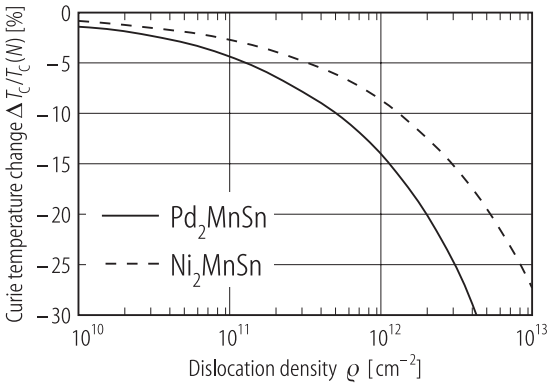

Fig. 113. Variation rate of the Curie temperature by plastic deformation, $\Delta T_C/T_C(N)$ in Pd_2MnSn and Ni_2MnSn. N refers to the normal undeformed state [84I1].

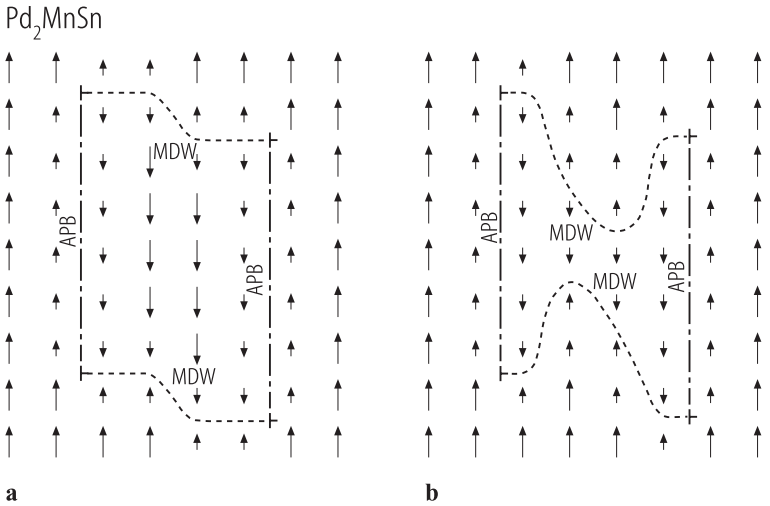

Fig. 114. Schematic explanation of the appearance of antiferromagnetic domains in the plastically deformed Pd_2MnSn alloys which are associated with the domains lying between the antiphase boundaries APB (*1*) with narrow width $R \leq R_c$. R_c is the critical width of the domain lying between APB's which the ferromagnetic domain begins to invade. The volume of this antiferromagnetic domain decreases more in magnetic fields, (**b**), than in zero fields, (**a**) [84I1]. MDW: magnetic domain wall.